Comparison of surface mass balance of ice sheets simulated by positive-degree-day method and energy balance approach

Eva Bauer, Andrey Ganopolski

Potsdam Institute for Climate Impact Research, Potsdam, Germany

Correspondence to: Eva Bauer (eva.bauer@pik-potsdam.de)

Abstract. Glacial cycles of the late Quaternary are controlled by the asymmetrically varying mass balance of continental ice sheets in the Northern Hemisphere. Surface mass balance is governed by processes of ablation and accumulation. Here two ablation schemes, namely the positive-degree-day (PDD) method and the surface energy balance (SEB) approach, are compared in transient simulations of the last glacial cycle with the Earth system model of intermediate complexity CLIMBER-2. It uses the SEB approach which comprises fluxes of short-wave and long-wave radiation, of sensible and latent heat and accounts explicitly for snow albedo changes from eolian dust deposition and snow aging. The standard version of the CLIMBER-2 model simulates ice volume variations in a reasonable agreement with paleoclimate reconstructions during the entire last glacial cycle. Using results of the standard CLIMBER-2 model for the last glacial cycle, we simulate ablation with the PDD method in off-line mode by applying different combinations of three empirical parameters of the PDD scheme. We found that none of the parameters combination allows us to simulate surface mass balance of American and European ice sheets similar to that obtained with the standard SEB method. The use of constant values of empirical PDD parameters lead either to too large ablation during the first phase of the last glacial cycle or to too little ablation during the final phase. We then substituted the standard SEB scheme in CLIMBER-2 by the PDD scheme and performed a suit of simulations of the last glacial cycle with different combinations of PDD parameters. Results of these simulations confirmed results of the off-line simulations: we failed to find a combination of PDD parameters which allow us to simulate realistically ice sheets evolution during the entire glacial cycle. The use of constant parameter values leads either to a buildup of too much ice volume at the end of glacial cycle or too little ice volume at the beginning. Even when the model correctly simulates global ice volume at the Last Glacial Maximum (21 ka), it is unable to simulate complete deglaciation during Holocene. According to our simulations, the SEB approach, including effects of changing snow albedo from dust deposition and aging, proves superior for simulation of glacial cycles.

1 Introduction

Glacial-interglacial cycles of the Quaternary are characterized by massive fluctuations of continental ice mass in the Northern Hemisphere (NH). These fluctuations result from gains and losses of ice mass through the interplay of the processes of snow accumulation and surface ice ablation and the dynamic processes of calving and basal melt. The sum of gains and losses of ice mass constitutes the net mass balance. During a glacial cycle, ice sheets typically build up relatively slowly over roughly four precessional periods until glacial maximum and thereafter they retreat rapidly over about ten millennia. In the initial phase of

a glacial cycle the accumulation predominates and ice sheets grow while at glacial termination the ablation predominates and ice sheets melt.

The net surface mass balance is the volumetric change across an entire ice sheet and across a full accumulation and melt season. On existing ice sheets or glaciers, the surface mass balance can be obtained from local measurements of the amounts of snow accumulated in winter and of snow and ice melted in summer. On long orbital time scales, the changing surface mass balance of the NH ice sheets is considered the main factor for the ice sheet evolution during a glacial cycle.

The net surface mass balance of ice sheets is equal to the difference between accumulation, which is controlled by the hydrological cycle, and of ablation which is determined by the surface energy balance (SEB). SEB primarily depends on absorption of insolation reaching the ice sheet surface and on temperature. Numerical modeling suggests that both the accumulation and the ablation of the major ice sheets in America and Europe vary in the range of 0.05 to 0.2 Sv ($1\,\mathrm{Sv} = 10^6\,\mathrm{m}^3\,\mathrm{s}^{-1}$) for most of glacial time period (Ganopolski et al., 2010). This means that the surface mass balance is highly sensitive to small changes in accumulation and ablation and a successful simulation of a glacial cycle evolution depends decisively on adequate descriptions of the accumulation and ablation processes. Difficulties to describe the processes arise from the nonlinear nature of the climate system and from insufficient data which are needed to constrain model parameters.

Two methods are widely used to simulate surface mass balance of ice sheets. One method is the so-called positive-degree-day (PDD) method. This semi-empirical parameterization requires information only about surface air temperature (usually, monthly mean values are used). This method is computationally fast and therefore widely used to simulate the surface mass balance of ice sheets both in past (Tarasov and Peltier, 1999, 2002; Zweck and Huybrechts, 2003, 2005; Charbit et al., 2007; Abe-Ouchi et al., 2007; Lunt et al., 2008; Gregoire et al., 2012; Beghin et al., 2014; Liakka et al., 2016) and in future climate simulations (van de Wal and Oerlemans, 1997; Huybrechts and de Wolde, 1999; Greve, 2000; Huybrechts et al., 2004; Ridley et al., 2005; Charbit et al., 2008; Winkelmann et al., 2015). The PDD method can be calibrated by use of measurements from glacier's surfaces but different glaciers give different values for the PDD scaling parameters.

The other method is the physical-based SEB method which computes from a surplus in the surface energy balance the melting of snow and ice in case the ice sheet surface temperature is above melting point. This method requires calculations of all components of the energy balance (short-wave and long-wave radiation, sensible and latent heat fluxes) which, in turn, requires a complete set of meteorological conditions. This method is computationally much more demanding than the PDD method and therefore was used till recently mostly in the framework of regional climate models for short-term climate predictions (Bougamont et al., 2006; Box et al., 2006, 2012; Fettweis, 2007, 2013; Ettema et al., 2009). However, simulations with a comprehensive Earth system model demonstrated that feedbacks between climate and ice sheets, which are not resolved by the PDD method, are important for simulating the ice mass balance of future climate change scenarios (Vizcaino et al., 2010).

In spite of the obvious advantages of the PDD method for modeling the long-term climate-ice sheet interaction, there is also a growing body of evidence that the PDD method is inadequate for modeling of Quaternary glacial cycles. One obvious problem is that the PDD method does not explicitly account for absorption of short-wave radiation which represents the fundamental energy component of the SEB. This can lead to significant underestimation of the effect from the varying insolation on orbital time scales which is seen the primary driver of the glacial cycles (Robinson et al., 2010; van de Berg et al., 2011; Ullman

et al., 2015). Another semi-empirical approach, namely ITM (Insolation-Temperature-Melt)scheme does explicitly account for absorption of insolation and reveals reasonable agreement with the SEB method in simulation of Greenland ice sheet surface mass balance for the Eemian interglacial (Robinson et al., 2011; Robinson and Goelzer, 2014). However, ITM requires prescription of 'atmospheric transmissivity' which is strongly spatially and temporally dependent and in general not known. In addition, ITM also does not account explicitly to the effect of dust deposition on surface albedo. This could be a serious disadvantage since paleoclimate data indicate significant increases of eolian dust deposition during glacial times, especially along the southern margins of the NH ice sheets (Kohfeld and Harrison, 2001; Mahowald et al., 2006). Both theoretical analysis (Warren and Wiscombe, 1980; Aoki et al., 2011) and direct measurements (Painter et al., 2010, 2012; Skiles et al., 2012; Bryant et al., 2013; Doherty et al., 2013, 2014; Gautam et al., 2013) demonstrate that even a small amount of impurities affects the surface albedo significantly. In turn, results from SEB simulations show that these changes in albedo might significantly affect the surface mass balance of ice sheets during glacial times (Krinner et al., 2006; Ganopolski et al., 2010) and in future climate change scenarios (Dumont et al., 2014; Goelles et al., 2015). At last, numerical parameters for the PDD method can only be derived from observations over the existing ice sheets, primarily Greenland, and it is unclear a priory how different such parameters should be when the PDD method is applied to completely different climate conditions and different geographical distributions of ice sheets during glacial times.

Charbit et al. (2013) discuss the effect of different PDD parameterizations on the NH ice sheet evolution, but a direct comparison between PDD and SEB approaches in a transient simulation over the glacial cycle with a climate-ice sheet model is missing. Here using results from ensemble transient simulations of the last glacial cycle performed with an Earth system model of intermediate complexity we undertake a systematic comparison of ice sheet surface mass balance simulated using SEB and PDD approaches for different ice sheets and during different periods of the last glacial cycle.

2 Model description

2.1 Model setup

The setup of the climate model CLIMBER-2 (Petoukhov et al., 2000; Ganopolski et al., 2001) for simulations of glacial cycles and its performance are described in Calov et al. (2005) and Ganopolski et al. (2010). This model is designed to investigate processes and their interactions in the Earth climate system over the long time scales, such as Quaternary glacial cycles, which is achieved at expense of complexity and spatial resolution. The model has been used already in glacial cycle simulations to study the 100 ka climatic cyclicity of the Quaternary (Ganopolski and Calov, 2011), the mineral dust cycle (Bauer and Ganopolski, 2010), the climate response to the dust radiative forcing (Bauer and Ganopolski, 2014) and the impact of permafrost on simulation of glacial cycles (Willeit and Ganopolski, 2015).

CLIMBER-2 consists of interactively coupled models for the atmosphere, the ocean, the land surface, the vegetation and the ice sheets. The atmospheric fields are computed on a longitude $\times$ latitude grid containing 7×18 grid cells. The 3-d polythermal ice sheet model SICOPOLIS operates on the NH between 21 and 85.5 °N on a longitude, latitude grid (x_s, y_s) with a resolution of (1.5 °, 0.75 °). Thus one atmospheric grid cell can overlap with more than 450 grid cells of the ice sheet model. CLIMBER-

2 computes the atmospheric fields with a daily time step, the oceanic fields every five days and the vegetation distribution every year. SICOPOLIS computes the ice sheet evolution from losses and gains of ice mass over a one-year period. The climate component and SICOPOLIS are coupled once per 10 years through the interface module SEMI (Surface Energy and Mass balance Interface). SEMI performes physically based 3-dimensional downscaling of climatological fields from coarse atmospheric grid to ice sheet model grid and computes the surface mass balance and the surface temperature using SEB approach with 3-day time step. Computed annual fields of surface ice sheet mass balance and of surface temperature are used in SICOPOLIS. In turn, SICOPOLIS feeds back to climate component the average ice sheet elevation, the fraction of land area covered by ice sheets, the sea level and the freshwater flux into the ocean from the ablation of ice sheets and from ice calving.

2.2 Surface energy and mass balance interface (SEMI)

The interface module SEMI computes the surface mass balance on the SICOPOLIS grid (Calov et al., 2005). The surface mass balance $F_{SEB}(x_s, y_s)$ is defined by

$$F_{SEB}(x_s, y_s) = P(x_s, y_s) - A_{SEB}(x_s, y_s) \tag{1}$$

where $P(x_s, y_s)$ is the snow accumulation and $A_{SEB}(x_s, y_s)$ is the surface ablation (positively defined) which is hereafter called SEB-derived ablation. In SEMI, prognostic equations for ice surface temperature and snow layer thickness are solved based on the surface energy balance. The SEB comprises short-wave and long-wave radiative fluxes and turbulent energy fluxes. These fluxes are calculated through horizontal and vertical interpolation of the fields of the coarse-resolution atmospheric component, as of insolation, solar incidence angle, longwave radiation, cloud fraction, air temperature, precipitation, and wind velocity.

A_{SEB} is computed from a surplus in SEB values which contains an explicit dependence on snow albedo. Here, snow albedo refers to broadband albedo composed of contributions from visible and near-infrared bands. Snow albedo is a function of snow aging and deposition of dust mass (Warren and Wiscombe, 1980). Effective snow age in CLIMBER-2 is a function of temperature and snow fall. Dust deposition is composed of aeolian dust transported from remote desert regions and of glaciogenic dust from glacial erosion Ganopolski et al. (2010). The computation of P includes the elevation-desert effect which causes decreasing P with increasing ice sheet elevation, and the elevation-slope effect which causes increasing P with increasing slope of the ice sheet surface. The slope effects also depends on the direction of average wind(Calov et al., 2005). Sublimation is neglected.

2.3 Positive-degree-day (PDD) method

The PDD-derived ablation A_{PDD} is calculated on the SICOPOLIS grid within the SEMI module. The PDD method is based on the reasoning that ablation is driven by the annual sum of positive temperature values which is seen as a proxy for melt energy (Braithwaite, 1984; Braithwaite and Olsen, 1989; Reeh, 1991). The semi-empirical PDD method is represented by a linear relationship using PDD values and proportionality factors for snow and ice melt. The PDD value (in $^\circ\mathrm{C\,d}$) is defined as excess of daily surface air temperature above the melting point accumulated over a year. Most implementations of the PDD

method take daily temperature values from interpolated monthly mean climatological data. To account for the missing diurnal cycle and synoptic variability, a temperature variability term is included because the short-term temperature variability may implicate melt occurrences, even if the mean temperature is negative.

The PDD value is computed from the integral over time t

$$PDD = \int_{\Delta t} dt \, [\frac{\sigma}{\sqrt{2\,\pi}} \, exp(-\frac{T^2}{2\,\sigma^2}) \, + \frac{T}{2} \, erfc(-\frac{T}{\sqrt{2}\,\sigma})] \tag{2}$$

where $\Delta t = 1\,\mathrm{year}$, T (in $^\circ\mathrm{C}$) is the climatological mean surface air temperature, $erfc(x)$ is the complementary error function and σ is the standard deviation of daily temperature from climatological mean value (Calov and Greve, 2005). Usually, σ is prescribed in the range 4.5-5.5 $^\circ\mathrm{C}$ (Reeh, 1991; Ritz et al., 1997; Tarasov and Peltier, 1999, 2002; Greve, 2005). Fausto et al. (2009) analyzed observations and showed that σ for the Greenland ice sheet may increase from 1.6 to 5.2 $^\circ\mathrm{C}$ for altitude increasing from 0 up to 3000 m.

The PDD-derived ablation is defined analogous to Eq. (1)

$$A_{PDD}(x_s, y_s) = P(x_s, y_s) - F_{PDD}(x_s, y_s) \tag{3}$$

where the description for $P(x_s, y_s)$ in Eq. (1) and Eq. (3) is unchanged. The surface mass balance F_{PDD} (in $\mathrm{mm\,y^{-1}}$) is calculated by

$$F_{PDD} = \begin{cases} \alpha_I \, Q & : \quad Q < 0 \\ 0 & : \quad Q = 0 \\ \alpha_S \, (1 - r_S) \, Q & : \quad Q > 0 \end{cases} \tag{4}$$

where α_S and α_I (in $\mathrm{mm\,^\circ C^{-1}\,d^{-1}}$) are the melt factors of snow and ice, respectively, and $r_S = 0.3$ is a constant refreezing factor. This factor is introduced for the nocturnal refreezing of snow and causes a slow down of the snow melt. The factor Q (in $^\circ\mathrm{C\,d\,y^{-1}}$) is the actual remain of PDD per year Δt

$$Q = \frac{PDD_S - PDD}{\Delta t} \tag{5}$$

where PDD is given in Eq. (2) and PDD_S is

$$PDD_S = \frac{P \, \Delta t}{\alpha_S \, (1 - r_S)} \tag{6}$$

which represents that PDD value which is required to melt the annual accumulated snow P. The sign of Q determines the sign of the surface mass balance F_{PDD}. When the PDD value (Eq. 2) is too small to melt the available snow then the remaining snow at the end of the year builds ice mass and F_{PDD} is positive. Reversely, when the PDD value is large enough to melt all snow in the grid cell then the remain Q (Eq. 5) melts surface ice and F_{PDD} is negative.

Values of the melt factors in the PDD scheme which are suitable for realistic simulation of ice sheets over the entire glacial cycle are not known (Hock, 2003). In the following, we attempted to find a unique set of three empirical parameters of the PDD

scheme which are optimal for this task. To this end we used PDD scheme to simulate ablation in the 'offline' mode and then in the 'online' mode. In the first case, the PDD scheme is used to calculate annual ablation rate in parallel with the standard SEB scheme employed in SEMI. Ablation simulated with the PDD scheme does not affect ice sheet evolution and is only used for comparison with the standard SEB scheme. Note than this approach is fully equivalent to the standard 'offline' technique, when temperature and precipitation fields are stored in the process of simulations with the standard CLIMBER-2 model and only then used to simulate surface mass balance with the PDD scheme. In the online mode, the SEB scheme of the SEMI module is disabled and ablation is computed with the PDD scheme. Note that in both cases (online and offline) accumulation is computed the same way but precipitation fields are not the same for these two methods because precipitation also depends on ice sheets distribution and elevation, which are not the same in online and offline simulations. Offline and online modes are both useful to compare different ablation schemes because in offline mode both schemes are forced by identical climate forcing but it does not tell how much differences in simulated ablation would affect ice sheet evolution. In the case of online simulation, comparison of two ablation schemes is complicated by strong nonlinearity of climate-cryosphere system where even small differences in the forcings can lead to dramatic differences in the system response on long time scales.

2.4 Reference simulation of the last glacial cycle

The reference simulation of the last glacial cycle is driven by the insolation calculated from the varying orbital parameters (Berger, 1978) and the time-varying concentration of greenhouse gases (Fig. 1a) expressed as equivalent CO_2 concentration (Ganopolski et al., 2010). The initial condition is the equilibrium climate state computed with greenhouse gas concentration and orbital forcing of the preindustrial period with the Greenland ice sheet as the only NH ice sheet. The shortwave radiative forcing by aeolian dust and the deposition of desert dust on snow of ice sheets are computed by use of time slice simulations from general circulation models. The horizontal fields of the time slices are transformed to temporally varying fields by scaling the time slices with the simulated ice volume (Calov et al., 2005) . The dust deposition on ice sheets includes further dust from internally simulated sediments produced by glacial erosion (Ganopolski et al., 2010). Note that in online simulations, both the dust radiative forcing and the snow albedo differ from that in offline experiment.

Figure 1b shows the reference time series of global mean surface air temperature and global mean precipitation over $130\,\mathrm{ka}$. The global temperature T decreases by more than $6\,^{\circ}\mathrm{C}$ from the Eemian interglacial until $21\,\mathrm{ka}$, the last glacial maximum (LGM). Subsequently, T rises rapidly by $5.5\,^{\circ}\mathrm{C}$ within about $10\,\mathrm{ka}$ until the early Holocene. The global precipitation is thermodynamically controlled and varies in close relationship to T (Fig. 1b). Figure 1c shows the mean sea level variation computed from the NH ice volume (assuming constant ocean surface area and an additional 10% contribution from the Antarctic ice sheet) in comparison to the global mean sea level from reconstructions (Waelbroeck et al., 2002).

Figure 2 shows the characteristics of the NH ice sheets by comparing NH total values with values from the American and the European ice sheets which represent, respectively, all ice sheets in North America and in Eurasia up to $120\,^{\circ}\mathrm{E}$. Note that the Greenland ice sheet is not included in the selections, but contributes to globally average values. . Up to $70\,\%$ of the total ice-covered area occurs in America and mostly less than $20\,\%$ occurs in Europe (Fig. 2a). The total ice volume, given in

meter sea level equivalent (msle), varies about proportional to the total ice sheet area (Fig. 2b). The area and the volume vary in parallel with the precession and obliquity-driven variations of the northern summer insolation.

Figure 2c shows areal averages of the time-varying ice sheet thickness. During the interglacial periods, the relatively high average ice thickness over NH is related to the persisting Greenland ice sheet. In the initial millennia of glacial inception, the drop in the average ice thickness results from the fast spreading of the ice sheet area during inception (Calov et al., 2005). Thereafter the average thickness of the American ice sheet grows, stays high beyond the LGM and drops rapidly toward to beginning of the Holocene. The European ice sheet thickness starts to grow at glacial inception a few millennia before the American ice thickness. Around the LGM, the European ice thickness increases by about 30 % which is accompanied with an extra cooling over the northern Atlantic. The lead of the thinning of the European ice sheet compared to American ice sheet at glacial termination is attributed to the lower elevation of the European ice sheet which facilitates the ice melt. Yet, during glacial termination the thinning of the American ice sheet occurs more rapidly than of the European ice sheet.

The time series of snow accumulation (Fig. 2d) and surface ablation (Fig. 2e) vary in comparable ranges. P is well correlated with the ice sheet area and varies with the precessional period in a rather linear manner. A_{SEB} varies in response to different driving factors, as insolation, surface ice area exposed to temperature above melting point and albedo of the snow surface. The maximum ablation after the LGM occurs in America some millennia earlier than in Europe. The lead of the maximum ablation in America is related to the larger perimeter exposed to melt conditions and the more southerly extent of the American ice sheet. The resulting surface mass balance (Fig. 2f) is positive and exceeds calving rate (not shown) during most of the last glacial cycle leading to the buildup of large NH ice sheets at the LGM.

3 Mass balance computed by PDD method in offline simulation

Since over the last glacial cycle empirical data needed to calibrate the PDD scheme are absent, we considered results of the standard, SEB-based mass balance simulations as the target for the PDD scheme. We compare ablation simulated by the PDD method with different empirical parameters with the results of the standard model version. We performed a large set of offline simulations with the PDD scheme where the standard deviation for temperature σ (Eq. 2) and melt factors α_S and α_I (Eq. 4) are considered as tunable parameters. Each simulation is run with constant parameter values over the entire glacial cycle.

3.1 Selection of PDD parameter values

The PDD value computed with the (Eq. 2) depends on prescribed standard deviation for temperature. In this study we used two different values , i.e., σ=3 °C and σ=5 °C. Figure 3 shows time series of T and the corresponding PDD values as areal averages over the ice sheets. After the Eemian at about 120 ka, the temperature averaged over the NH ice sheet area decreases by 13 °C (from -16 to -29 °C) in a time interval of nearly 100 ka and then T recovers rapidly within about 10 ka (Fig. 3a). The PDD values are closely correlated with T showing a progressive decrease after glacial inception and a rapid increase during glacial termination. The averages of the PDD value for the total ice sheet lie in the ranges 10–70 and 20–120 °C d with σ=3 and 5 °C, respectively (Fig. 3a). The glacial cycle asymmetry is substantiated by the massive and widespread ice sheet in

America which shows a temperature evolution from -16 to -27 °C (Fig. 3b). The temperature of the smaller European ice sheet fluctuates more strongly, i.e. from -10 to -29 °C. These fluctuations are connected with changes in the sea-ice albedo effect in the northern Atlantic and changes of the Atlantic meridional overturning circulation. The PDD values for Europe range over 10–260 °C d with σ=3 °C and over 30–370 °C d with σ=5 °C (Fig. 3c).

Previous climate model studies often used σ =5 °C and so-called standard melt factors for snow and ice which are (α_S, α_I) = (3, 8) mm °C^{-1} d^{-1} as derived from measurements on the Greenland ice sheet (Huybrechts and de Wolde, 1999; Tarasov and Peltier, 1999, 2000). However, other observations show that melt factors may vary with latitude and height of the glacier. Hock (2003) summarized worldwide measurements during the melt season of glaciers and snow-covered basins and showed that (α_S, α_I) may vary in the ranges ([2.5–11.6], [5.4–20]) mm °C^{-1} d^{-1}. The ranges of the melt factors are relatively wide because they are obtained from different environments and incorporate variations in space and time, insolation, ice sheet elevation, sensible heat flux and surface albedo. Here, we consider two σ values to test the possible effect on A_{PDD} from unresolved space-time variations in the modeled temperature. For each σ value, the values for α_S and α_I are varied in wide ranges. In case σ=3 °C, (α_S, α_I) are varied in the ranges ([3-10], [8-24]) mm °C^{-1} d^{-1}, and in case σ=5 °C in the ranges ([2-6], [4-18]) mm °C^{-1} d^{-1}. Thus the offline PDD-derived ablation can capture the entire variability of the simulated SEB-derived ablation during the glacial cycle.

3.2 Ablation time series for ice sheets over glacial cycle

In an attempt to find PDD parameter values which produce the best fit to A_{SEB}, we calculate as measures of agreement the mean anomaly m and the rms–error r from time series of ablation averaged over ice sheets. Figure 4 shows contour plots of m and r as function of α_S and α_I calculated from 130 ka-long series of A_{PDD} and A_{SEB} for the all NH ice sheets. For both σ values, no unique pair of (α_S, α_I) values exists at the minimum in m (Fig 4a, c) while the minimum in r can be associated with a specific pair of (α_S, α_I) values (Fig. 4b, d). However, the minimum rms-error of about 0.025 Sv is large and amounts to more than 50% of the peak value in A_{SEB} simulated at 15 ka. In another attempt, we try to find optimal PDD parameter values separately for the American and the European ice sheets. The contour plots of the rms–error as a function of α_S and α_I (Fig. 5) show that very different values of (α_S, α_I) are optimal for American and European ice sheets (Tab. 1). Overall, r for the American ice sheet (Fig. 5a, c) is about a factor three larger than for the European ice sheet (Fig. 5b, d) in both σ-sets.

Figure 6 shows the PDD-derived ablation evolution for the American and the European ice sheets for the entire ensemble together with the SEB-derived ablation. The agreement between the series is much lower for the American than for the European ice sheets irrespective of the σ value. Typically A_{PDD} and A_{SEB} agree better during glacial inception then A_{PDD} underestimates the peak in A_{SEB} at glacial termination and, reversely, if A_{PDD} reproduces the peak in A_{SEB} at glacial termination then A_{PDD} overestimates A_{SEB} at glacial inception. Hence, smaller melt factors would be needed for glacial inception than for glacial termination. So, we divide the time series into the intervals 130–30 ka and 30–0 ka and determine for each sub-interval the PDD parameter values which minimize the rms–error (Tab. 1). Nonetheless, ablation series fitted for the American ice sheet and for sub-intervals diverge repeatedly from the reference series (Fig. 6a, c). In particular, the enhanced ablation from the American ice sheet during MIS 4 (ca. 75-60 ka) is difficult to reproduce with the PDD method. Otherwise,

the PDD-derived ablation series fitted for the European ice sheet for sub-intervals agree quite well with the reference and the discontinuity at 30 ka is small (Fig. 6b, d).

3.3 Geographical resolved ablation rates at 15 ka

At 15 ka, the total SEB-derived ablation reaches its maximum of 0.41 Sv (Tab. 2).This is why we choose this time slice to analyze geographical distribution of ablation simulated with the PDD scheme versus the standard SEB approach. The ensemble member which produces similar total ablation as in the reference simulation at 15 ka is obtained with (α_S, α_I)=(9, 16) $\mathrm{mm\,^{\circ}C^{-1}\,d^{-1}}$ and σ=3 °C (Fig. 7).

Figure 8 compares the spatial patterns of ablation rates simulated with both methods on the SICOPOLIS grid using the ensemble which produces the same NH total ablation as the reference simulation at 15 ka (Fig. 7). The scatter diagram shows that the PDD method tends to overestimate large ablation rates and to underestimate low ablation rates. The PDD-derived American melt rates overestimate the reference melt rates larger than $\sim$10 $\mathrm{mm\,d^{-1}}$ but underestimate the American ice melt rates less than $\sim$8 $\mathrm{mm\,d^{-1}}$ (Fig. 8a). The PDD-derived European melt rates are overestimated mainly for ablation rates larger than $\sim$6 $\mathrm{mm\,d^{-1}}$ (Fig. 8b). The largest ablation rates occur naturally at the ice sheet margins and here the largest differences occur. This is evident from the geographic distribution of the differences between the PDD-derived ablation relative to the SEB-derived ablation at 15 ka (Fig. 9). The differences are positive mostly at the outer margins of the ice sheets. Negative differences occur predominately around the Rocky Mountains.

4 Glacial cycle simulations with online PDD method

Above we evaluated PDD-derived ablation from offline simulations against the SEB-derived ablation. In doing so we explicitly assumed that the latter gives realistic spatial and temporal distribution of ablation since in the reference simulation ice sheets evolution during the last glacial cycle is in reasonably good agreement with paleoclimate reconstructions. We found that ablation simulated with the PDD scheme in general deviates appreciably from that simulated with the standard SEB approach. To asses how these differences will influence ice sheet evolution during the last glacial cycle, we performed a set of PDD-online simulations, where the PDD scheme for ablation replaces the standard SEB scheme. Note, that the scheme for simulations of accumulation remains the same in these simulations. We evaluate the PDD-online simulation by comparing their results with the reconstructed global sea level and climate characteristics from the reference simulation.

4.1 Selection of PDD parameters values

A few dozens of glacial cycle simulations with online application of the PDD method were performed. In these experiments we tested how well evolution of ice sheets and climate can be simulated with constant PDD parameters values. It appears that the values of three PDD parameters can be tuned adequately for certain time periods but not for the entire glacial cycle. The PDD online simulations can be split into two clusters. In the first one, the temperature and the sea level are reasonably simulated during glacial inception (from 120 ka until about 110 ka) but diverge dramatically from paleoclimate reconstructions for the

rest of glacial cycle. In particular, all these simulations fail to simulate deglaciation toward the end of Holocene. Simulations of the second cluster are able to simulate complete deglaciation before the end of the experiment and reproduce the climate of the Holocene realistically but significantly underestimate ice sheets volume during most of glacial cycle. In the following, we show representative simulations from the two clusters with parameter values given in Tab. 3. The target periods inception and termination are seen to impose a rather weak constraint for selecting the PDD parameter values. In contrast, the target period LGM (21 ka) emerged as a rather strong empirical constraint. Only one specific pair of melt factors values for each σ value (Tab. 3) is found suitable to simulate the LGM climate with the online PDD method.

4.2 Target periods: glacial inception and termination

During glacial inception (from about 120 ka until 110 ka, PDD-online simulations I3 and I5 (Tab. 3) reproduce closely the global temperature (Fig. 10a, c) and the sea level (Fig. 10b, d). In this time interval, the ice sheet area grows sufficiently fast in company with accumulation. The reproduction of T implies reproductions of both the ice sheet thickness and the ablation and consequently the surface mass balance agrees with the reference (not shown). Thereafter the ice volume grows too fast in concert with amplified snow accumulation and the simulation drifts into excessive cold climate. At 21 ka, in these experiments the ice volume is about twice as large as reconstructed (Tab. 3) and simulations I3 and I5 fail to terminate the glacial climate state.

Contrary to the experiments described above, the temperature and the sea level in simulations T3 and T5 simulate realistically the Holocene climate characteristics after a weak glacial phase (Tab. 3). The global cooling after inception is about in phase with the reference temperature though the cooling in the PDD-online simulations is substantially underestimated (Fig. 10a, c). The sea level drop in simulation T3 is about half as large as reconstructed over the glacial phase (Fig. 10b) and in simulation T5, the maximum sea level drop of 40 m occurs after the LGM (Fig. 10d). From 38 to 20 ka the cooling rate in both simulations T3 and T5 intensifies and thereby the ice volume grows continuously beyond 21 ka until around 18 ka. The recurrence to Holocene climate begins from a less cool climate and a smaller ice-covered area than in the reference experiment. Therefore, both simulations T3 and T5 undershoot the buildup of the ice volume substantially.

4.3 Target period: LGM

PDD-online simulations L3 and L5 reproduce reasonably well the reconstructed sea level at 21 ka (Tab. 3). In the initial phase of the glacial cycle, simulation L3 produces a weaker cooling and less ice volume than the reference but in the time interval 40–21 ka the agreement is close (Fig. 10a, b). Simulation L5 generates a growing ice volume over the entire glacial phase which agrees well within uncertainties inferred from the reference and the reconstructed sea level (Fig. 10c, d). However, in simulations L3 and L5, the ice volume grows beyond 21 ka by several msle. The continued growth of the ice volume is caused by a continued positive mass balance from less ablation than in the reference simulation, mainly in America. Consequently, glacial termination is delayed and the recurrence to Holocene climate characteristics is not achieved.

The geographic distribution of the ice sheet thickness at 21 ka from PDD-online simulation L3 agrees closely with the reference simulation (Fig. 11). Simulation L3 reproduces the maximum thickness of 3500 m in America as simulated by the

reference but in simulation L3 the ice sheet spreads slightly more southward beyond the American Great Lakes and the ice sheet in the European Arctic and in northeastern Asia is slightly thinner. Also, simulation L5 produces an ice sheet distribution similar to the reference although the maximum thickness in America is only 3300 m at LGM. Both PDD-online simulations L3 and L5 simulate at LGM a sea level of -120 m, but thereafter their mass balances remain more positive than in the reference which results in lagged climate warming and in case of simulation L5 the deglaciation is incomplete (ca. 50 msle remain at present).

5 Impact of snow albedo parameterizations on simulated surface mass balance and ice sheet evolution

In nature, ablation is largest when insolation reaches a maximum and when the surface temperature is above freezing. Hence, ablation zones are highly localized in time and space and ablation occurs only in summer at ice sheet margins. In the reference simulation, ablation is computed by SEMI module based on the physically-based SEB approach. Snow albedo parameterization is one of the key elements of the SEMI module. To demonstrate the importance of proper parameterization of snow albedo we performed additionally a set of experiments where we split the function describing snow albedo into its components to test their individual effect on ablation. In doing so, we run again offline and online simulations of the last glacial cycle with the CLIMBER-2 model. Three components in the parameterization of snow albedo used in the SEMI module are critically important, namely, the aging of pure snow depending on temperature, the concentration in snow of light-absorbing impurities from dust deposition and the synergy between aging of snow and impurities (Warren, 1982; Warren and Wiscombe, 1980). Under 'synergy' we understand here the fact that the effect of impurities on snow albedo is much higher for the 'old' snow than for the fresh snow. We select four test cases where snow albedo is defined in C1 as pure snow without aging (snow remains fresh), in C2 as snow with dust deposition but without snow aging (impure snow remains fresh), in C3 as pure snow with snow aging, and in C4 as with effect of dust deposition and snow aging but without the synergy between aging and dust deposition. (Tab. 4).

We first performed a set of offline simulations in which surface mass balance was computed for different snow albedo parameterizations using results of the reference experiments. In these experiments, the perturbed mass balance does not affect climate and ice sheet simulations and is used only for comparison with mass balance simulated in the reference experiemnt. Fig. 12 shows characteristic time series over the last glacial cycle obtained from the offline simulations in comparison to the reference simulation. These time series are shown as monthly means for June and July averaged over the NH ice sheets. The modified descriptions of snow albedo according to the four cases lead to substantial changes in co-albedo. Although the insolation in June is larger than in July (Fig. 12a, e), the ablation in July is more than 60 % larger than in June (Fig. 12d, h). The larger June insolation is accompanied by a lower co-albedo (Fig. 12b, f) such that the absorbed shortwave radiation in June and July are similar (not shown). The test case C1 imposes the maximum effect and causes a reduction in the co-albedo by about 30 % relative to the reference experiment. Case C2 shows that the dust-induced darkening effect is roughly proportional to ice volume. Case C3 however shows, that the aging effect from growing snow grain sizes has a larger effect than the dust-darkening in case C2. Only around LGM, the dust-induced effect is larger than the pure snow aging effect. Case C4 shows, that

neglecting the synergy between aging and impurities effect on albedo leads to a reduction in co-albedo by about 10 % relative to the reference experiment.

Fig. 13 compares the reference simulation with the online simulations from the four cases (Tab. 4). In these experiments changes in parameterization of surface albedo directly affected ice sheet evolution. Note that in these experiments we did not change parameterization of snow albedo in climate component of CLIMBER-2. Common to all four online simulations is that the climate cools extremely in accompany with excessive buildup of ice volume such that eventually no recovery to interglacial climate is achieved. Simulation C4 without the synergy between aging and impurities effect on snow albedo is the closest to the reference experiment but still about 150 msle of ice remains at 0 ka. Simulation C3 without dust deposition but accounting for snow aging produces a reasonable climate until only 120 ka. This is due to the interglacial climate condition in which ice sheets are not yet existing and dust deposition plays no role. In simulation C2 with dust deposition but without snow aging the climate begins to cool immediately after the start of the simulation. After about 100 ka, the effect of dust deposition is substantial and the cooling attenuates in comparison to simulation C3. Simulation C1 in which the snow albedo is computed for fresh and pure snow an excessive ice sheet builds up in Asia such that the model crashed already at 86 ka.

These first-order estimates of factors influencing the snow albedo discussed for the total NH ice sheets are depending on our model setup and further investigations with more advanced parameterizations (Dang et al., 2015) are desirable. In particular, recent observations of the Greenland ice sheet indicate a strong effect on surface albedo decline from the combination of climate warming, growth of snow grains and the accumulation of light-absorbing impurities (Tedesco et al., 2016).

6 Conclusions

The changing in space and time surface ice sheets mass balance plays a crucial role in shaping the glacial cycles of the Quaternary. Here, using the Earth system model of intermediate complexity CLIMBER-2 with a rather coarse resolution climate component we studied whether a simple and computationally efficient PDD scheme can satisfactorily emulate the much more complex and computationally demanding SEB-based scheme implemented in CLIMBER-2. To this end we performed a large set of experiments in offline and online modes. Ablation in offline mode is computed with the same climate forcing as in the reference simulation that allows a direct comparison of ablation series simulated by PDD and SEB schemes. By doing this comparison we assumed that reference simulation of the CLIMBER-2 model with the SEB approach is sufficiently realistic since the model simulates evolution of climate and ice sheets rather realistically. At the same time, climate component of the model has a rather coarse spatial resolution and sophisticated downscaling to ice sheet model grid includes a number of tunable parameters not all of them well constrained by empirical data. Therefore our comparison between SEB and PDD approached should be considered as tentative and using of higher resolution climate models would be desirable to make a final conclusion.

In summary, the offline simulated ablation by the PDD method with constant parameter values and the ablation simulated with the SEB approach are not compatible over the last glacial cycle. Hence, a use of the PDD method in case of large climate changes and geographically varying continental ice sheets, as observed in NH during a glacial cycle, is found problematic. Our study suggests that for realistic simulation of glacial termination, larger PDD melt factors are required than for glacial

inception, and also larger melt factors for the American ice sheet compare to the European one. In general, it appears that mass balance of European ice sheet is better correlated with the positive temperature sum than the American ice sheet. This suggests that the evolution of the American ice sheet is more strongly influenced by changes in absorbed shortwave radiation and surface albedo.

Online simulations with the PDD method show that no universal PDD parameter values are found by which the entire glacial cycle is simulated satisfactorily. Different, although not unique, PDD parameter values are required for reproducing the reconstructed sea level at glacial inception and at glacial termination. However, PDD-online simulations which generate a plausible sea level drop at glacial inception strongly overshoot thereafter the sea level drop at LGM and fail to recover to the interglacial sea level. PDD-online simulations where the Holocene sea level is correctly reproduce, too little ice is simulated during glacial inception. One set of PDD parameters is found by which the sea level is simulated quite well during the glacial phase and at LGM. After the LGM, however, the ice volume grows further during several millennia and subsequently the sea level at present is about $50\,\mathrm{msle}$ below observed one.

The reference simulation with the SEB approach suggests that the relatively fast spreading of the ice sheet area at glacial inception and the snow albedo changes from dust deposition at termination are important elements for the glacial cycle evolution. Further simulations with the SEB approach to analyze the factors influencing snow albedo show that dust deposition has a twofold impact on snow melt. Dust deposition itself causes a reduction in snow albedo which is additionally affected by the synergy between aging of snow and impact of impurities on snow albedo. Admittedly, the influences of dust radiative forcing and dust deposition on snow over ice sheet are included in a rather simplified manner in the current CLIMBER-2 model version. We hope that this study will motivates further investigations on the effect of eolian dust on snow albedo for climate-ice sheet interaction.

Acknowledgements. E.B. acknowledges support by the German Climate Modeling Initiative grant PalMod. Comments by two anonymous reviewer are greatly acknowledged.

References

Abe-Ouchi, A., Segawa, T., and Saito, F.: Climatic Conditions for modelling the Northern Hemisphere ice sheets throughout the ice age cycle, Clim. Past, 3, 423–438, doi:10.5194/cp-3-423-2007, 2007.

Aoki, T., Kuchiki, K., Niwano, M., Kodama, Y., Hosaka, M., and Tanaka, T.: Physically based snow albedo model for calculating broadband albedos and the solar heating profile in snowpack for general circulation models, J. Geophys. Res., 116, D11114, doi:10.1029/2010JD015507, 2011.

Bauer, E. and Ganopolski, A.: Aeolian dust modeling over the past four glacial cycles with CLIMBER-2, Glob. Planet. Change, 74, 49–60, 2010.

Bauer, E. and Ganopolski, A.: Sensitivity simulations with direct shortwave radiative forcing by aeolian dust during glacial cycles, Clim. Past, 4, 1333–1348, 2014.

Beghin, P., Charbit, S., Dumas, C., Kageyama, M., Roche, D. M., and Ritz, C.: Interdependence of the growth of the Northern Hemisphere ice sheets during the last glaciation: the role of at- mospheric circulation, Clim. Past, 10, 345–358, doi:10.5194/cp- 10-345-2014, 2014.

Berger, A. L.: Long-term variations of daily insolation and Quaternary climatic changes, J. Atmos. Sci., 35, 2362–2367, 1978.

Bougamont, M., Bamber, J., L., and Greuell, W.: A surface mass balance model for the Greenland Ice Sheet, J. Geophys. Res., 110, F04018, doi:10.1029/2005JF000348, 2005.

Box, J. E., Bromwich, D. H., Veenhuis, B. A., Bai, L.-S., Stroeve, J. C., Rogers, J. C., Steffen, K., Haran, T., and Wang, S.-H.: Greenland Ice Sheet Surface Mass Balance Variability (1988–2004) from Calibrated Polar MM5 Output, J. Climate, 19, 2783–2800, doi:10.1175/JCLI3738.1, 2006.

Box, J. E., Fettweis, X., Stroeve, J. C., Tedesco, M., Hall, D. K. and Steffen, K.: Greenland ice sheet albedo feedback: Thermodynamics and atmospheric drivers, Cryosphere, 6(4), 821–839, doi:10.5194/tc-6-821-2012, 2012.

Braithwaite, R.J.: Calculation of degree-days for glacier–climate research, Z. Gletscherkunde und Glazialgeologie, 20, 1–8, 1984.

Braithwaite, R.J. and O.B. Olesen: Calculation of glacier ablation from air temperature, West Greenland, Springer Netherlands, 219–233, 1989.

Braithwaite, R. J.: Positive degree-day factors for ablation on the Greenland ice sheet studies by energy-balance modelling, J. Glaciol., 41, 153–160, 1995.

Bryant, A. C., Painter, T. H., Deems, J. S., and Bender, S. M.: Impact of dust radiative forcing in snow on accuracy of operational runoff prediction in the Upper Colorado River Basin, Geophys. Res. Lett., 40, doi:10.1002/grl.50773, 2013.

Calov, R., and Greve, R.: Correspondence, J. Glaciol. 172, 173–188, 2005.

Calov, R., Ganopolski, A., Claussen, M., Petoukhov, V., and Greve, R.: Transient simulation of the last glacial inception – Part I: glacial inception as a bifurcation in the climate system, Clim. Dynam., 24, 545–561, 2005.

Charbit, S., Ritz, C., Philippon, G., Peyaud, V., and Kageyama, M.: Numerical reconstructions of the Northern Hemisphere ice sheets through the last glacial-interglacial cycle, Clim. Past, 3, 15–37, doi:10.5194/cp-3-15-2007, 2007.

Charbit, S., Paillard, D. and Ramstein, G.: Amount of CO2 emissions irreversibly leading to the total melting of Greenland, Geophys. Res. Lett., 35, L12503, doi:10.1029/2008GL033472, 2008.

Charbit, S., Dumas, C., Kageyama, M., Roche, D. M., Ritz, C.: Influence of ablation-related processes in the build-up of simulated Northern Hemisphere ice sheets during the last glacial cycle, The Cryosphere, 7, 681–698, 2013.

Dang, C., Brandt, R. E., and Warren, S. G.: Parameterizations for narrowband and broadband albedo of pure snow and snow containing mineral dust and black carbon, J. Geophys. Res. Atmos., 120, 5446–5468, doi:10.1002/2014JD022646, 2015.

Doherty, S. J., Grenfell, T. C., Forsström, S., Hegg, D. L., Brandt, R. E., and Warren, S. G.: Observed vertical redistribution of black carbon and other insoluble light-absorbing particles in melting snow, J. Geophys. Res. Atmos., 118, 5553–5569, doi:10.1002/jgrd.50235, 2013.

Doherty, S. J., Dang, C., Hegg, D. A., Zhang, R., and Warren, S. G.: Black carbon and other light-absorbing particles in snow of central North America, J. Geophys. Res. Atmos., 119, 12,807–12,831, doi:10.1002/2014JD022350, 2014.

Dumont, M., Brun, E., Picard, G., Michou, M., Libois, Q., Petit, J. R., Geyer, M., Morin, S., and Josse, B.: Contribution of light-absorbing impurities in snow to Greenland's darkening since 2009, Nat. Geosci., 7, 509–512, doi:10.1038/ngeo2180, 2014.

Ettema, J., van den Broeke, M. R., van Meijgaard, E., van de Berg, W. J., Bamber, J. L., Box, J. E., and Bales, R. C.: Higher surface mass balance of the Greenland ice sheet revealed by high-resolution climate modeling, Geophys. Res. Lett., 36, L12501, doi:10.1029/2009GL038110, 2009.

Fausto, R. S., Ahlstrøm, A. P., van As, D., Johnsen, S. J., Langen, P. L., and Steffen, K.: Improving surface boundary conditions with focus on coupling snow densification and meltwater retention in large-scale ice-sheet models of Greenland, J. Glaciol., 55(193), 869–878, 2009.

Fettweis, X.: Reconstruction of the 1979–2006 Greenland ice sheet surface mass balance using the regional climate model MAR, The Cryosphere, 1, 21–40, doi:10.5194/tc-1-21-2007, 2007.

Fettweis, X., Franco, B., Tedesco, M., van Angelen, J. H., Lenaerts, J. T. M., van den Broeke, M. R. and Gallee, H.: Estimating Greenland ice sheet surface mass balance contribution to future sea level rise using the regional atmospheric climate model MAR, The Cryosphere, 7, 469–489, 2013.

Ganopolski, A. and Calov, R.: The role of orbital forcing, carbon dioxide and regolith in 100 kyr glacial cycles, Clim. Past, 7, 1415–1425, doi:10.5194/cp-7-1415-2011, 2011.

Ganopolski, A., Petoukhov, V., Rahmstorf, S., Brovkin, V., Claussen, M., Eliseev, A., and Kubatzki, C.: CLIMBER-2: a climate system model of intermediate complexity. Part II: model sensitivity, Clim. Dynam., 17, 735–751, 2001.

Ganopolski, A., Calov, R., and Claussen, M.: Simulation of the last glacial cycle with a coupled climate ice-sheet model of intermediate complexity, Clim. Past, 6, 229–244, doi:10.5194/cp-6-229–2010, 2010.

Gautam R., Hsu, N. C., Lau, W. K.-M., and Yasunari, T. J.: Satellite observations of desert dust-induced Himalayan snow darkening, Geophys. Res. Lett., 40, 988–993, doi:10.1002/grl.50226, 2013.

Goelles, T. Bòggild, C. E. and Greve, R.: Ice sheet mass loss caused by dust and black carbon accumulation, The Cryosphere, 9, 1845–1856, doi:10.5194/tc-9-1845-2015, 2015.

Gregoire, L. J., Payne, A. J., and Valdes, P. J.: Deglacial rapid sea level rises caused by ice-sheet saddle collapses, Nature, 487, 219–223, 2012.

Greve, R.: A continuum-mechanical formulation for shallow polythermal ice sheets, Philos. T. Roy. Soc. Lond. A, 335, 921–974, 1997.

Greve, R.: On the response of Greenland ice sheet to greenhouse climate change, Clim. Change, 46, 289–303, 2000.

Greve, R.: Relation of measured basal temperatures and the spatial distribution of the geothermal heat flux for the Greenland ice sheet, Ann. Glaciol., 42, 424–432, 2005.

Hock, R.: Temperature index melt modelling in mountain areas, J. Hydrol., 282, 104–115, 2003.

Huybrechts, P. and de Wolde, J.: The dynamic response of the Greenland and Antarctic ice sheets to multiple century climatic warming, J. Climate, 12, 2169–2188, 1999.

Huybrechts, P., Gregory, J., Janssens, I., and Wild, M.: Modelling Antarctic and Greenland volume changes during the 20th and 21st centuries forced by GCM time slice integrations, Glob. Planet. Change, 42, 83–105, 2004.

Kleman, J., Fastook, J., Ebert, K., Nilsson, J., and Caballero, R.: Pre-LGM Northern Hemisphere ice sheet topography, Clim. Past, 9, 2365–2378, doi:10.5194/cp-9-2365-2013, 2013.

Kohfeld, K. E. and Harrison, S. P.: DIRTMAP: the geological record of dust, Earth-Sci. Rev., 54, 81–114, 2001.

Krinner, G., Boucher, O., and Balkanski, Y.: Ice-free glacial northern Asia due to dust deposition on snow, Clim. Dynam., 27, 613–625, 2006.

Liakka, J., Löfverström, M., and Colleoni, F.: The impact of the North American glacial topography on the evolution of the Eurasian ice sheet over the last glacial cycle, Clim. Past, 12, 1225–1241, doi:10.5194/cp-12-1225-2016, 2016.

Lunt, D. J., Valdes, P. J., Haywood, A., and Rutt, I. C.: Closure of the Panama Seaway during the Pliocene: implications for climate and Northern Hemisphere glaciation, Clim. Dyn. 30, 1–18, 2008.

Mahowald, N. M., Muhs, D. R., Levis, S., Rasch, P. J., Yoshioka, M., Zender, C. S., and Luo, C.: Change in atmospheric mineral aerosols in response to climate: Last glacial period, preindustrial, modern, and doubled carbon dioxide climates, J. Geophys. Res., 111, D10202, doi:10.1029/2005JD006653, 2006.

Painter, T. H., Deems, J. S., Belnap, J., Hamlet, A. F., Landry, C. C., and Udall, B.: Response of Colorado River runoff to dust radiative forcing in snow, Proc. Natl. Acad. Sci. U. S. A., 107, 17,125–17,130, doi:10.1073/pnas.0913139107, 2010.

Painter, T. H., Skiles, S. M., Deems, J. S., Bryant, A. C., and Landry C. C.: Dust radiative forcing in snow of the Upper Colorado River Basin: 1. A 6 year record of energy balance, radiation, and dust concentrations, Water Resour. Res., 48, W07521, 2012.

Reeh, N.: Parameterization of melt rate and surface temperature on the Greenland ice sheet, Polarforschung, 59(3), 113–128, 1991.

Petoukhov, V., Ganopolski, A., Brovkin, V., Claussen, M., Eliseev, A., Kubatzki, C., and Rahmstorf, S.: CLIMBER-2: a climate system model of intermediate complexity. Part I: model description and performance for present climate, Clim. Dynam., 16, 1–17, 2000.

Ridley, J. K., Huybrechts, P., Gregory, J.M., Lowe, J.A.: Elimination of the Greenland ice sheet in a high CO2 climate, J. Climate, 18, 3409–3427, 2005.

Ritz, C., Fabre, A., and Letréguilly, A.: Sensitivity of a Greenland ice sheet model to ice flow and ablation parameters: consequences for the evolution through the last climatic cycle, Clim. Dynam., 13, 11–24, 1997.

Robinson, A., Calov, R., and Ganopolski, A.: An efficient regional energy-moisture balance model for simulation of the Greenland Ice Sheet response to climate change, The Cryosphere, 4, 129–144, doi:10.5194/tc-4-129-2010, 2010.

Robinson, A., Calov, R., and Ganopolski, A.: Greenland ice sheet model parameters constrained using simulations of the Eemian Interglacial, Clim. Past, 7, 381–396, doi:10.5194/cp-7-381-2011, 2011.

Robinson, A., and Goelzer, H.: The importance of insolation changes for paleo ice sheet modeling, The Cryosphere, 8, 11419–1428, doi:10.5194/tc-8-1419-2014, 2014.

Skiles, S. M., Painter, T. H., Deems, J. S., Bryant, A. C., and Landry, C. C.: Dust radiative forcing in snow of the Upper Colorado River Basin: 2. Interannual variability in radiative forcing and snowmelt rates, Water Resour. Res., 48, W07522, doi:10.1029/2012WR011986, 2012.

Tarasov, L. and Peltier, W. R.: Impact of thermomechanical ice sheet coupling of the 100 kyr ice age cycle, J. Geophys. Res., 104, 9517–9545, 1999.

Tarasov, L. and Peltier, W. R.: Laurentide ice sheet aspect ratio in Glen's flow law, Annals of Glaciology, 30, 177–186, 2000.

Tarasov, L., and Peltier, W. R.: Greenland glacial history and local geodynamic consequences, Geophys. J. Int., 150(1), 198–229, 2002.

Tedesco, M., Doherty, S., Fettweis, X., Alexander, P., Jeyaratnam, J. and Stroeve, J.: The darkening of the Greenland ice sheet: Trends, drivers, and projections (1981–2100), The Cryosphere, 10, 477–496, doi:10.5194/tc-10-477-2016, 2016.

Ullman, D. J., Carlson, A. E., Anslow, F. S., LeGrande, A. N., Licciardi, J. M.: Laurentide ice-sheet instability during the last deglaciation, Nat. Geosci., 8, 534–537, 2015.

van de Berg, W. J., van den Broeke, M., Ettema, J., van Meijgaard, E., and Kaspar, F.: Significant contribition of insolation to Eemian melting of the Greenland ice sheet, Nat. Geosci., 4, 679–683, doi:10.1038/ngeo1245, 2011.

van de Wal, R. S. W., and Oerlemans, J.: Modelling the short-term response of the Greenland ice-sheet to global warming, Clim, Dynam., 13, 733–744, 1997.

Vizcaino, M., Mikolajewicz, U., Jungclaus, J., and Schurgers, G.: Climate modification by future ice sheet changes and consequences for ice sheet mass balance, Clim. Dyn., 34(2–3), 30–324, doi:10.1007/S00382-009-0591-Y, 2010.

Waelbroeck, C., Labeyrie, L., Michel, E., Duplessy, J., McManus, J., Lambeck, K., Balbon, E., and Labracherie, M.: Sea-level and deep water temperature changes derived from benthic foraminifera isotopic records, Quat. Sci. Rev., 21, 295–305, 2002.

Warren, S. G.: Optical properties of snow, Rev. Geophys., 20, 67–89, 1982.

Warren, S. G. and Wiscombe, W. J.: A model for the spectral albedo of snow. II: snow containing atmospheric aerosols, J. Atmos. Sci., 37, 2734–2745, 1980.

Willeit, M. and Ganopolski, A.: Coupled Northern Hemisphere permafrost-ice-sheet evolution over the last glacial cycle, Clim Past, 11, 1165–1180, 2015.

Winkelmann, R., Levermann, A., Ridgwell, A., and Caldeira, K.: Combustion of available fossil fuel resources sufficient to eliminate the Antarctic Ice Sheet, Science advances 1.8, 2015.

Zweck, C., and Huybrechts, P.: Modeling the marine extent of northern hemisphere ice sheets during the last glacial cycle, Ann. Glaciol., 37, 173–180, 2003.

Zweck, C., and Huybrechts, P.: Modeling of the northern hemisphere ice sheets during the last glacial cycle and glaciological sensitivity, J. Geophys. Res., 110, D07103, doi:10.1029/2004JD005489, 2005.

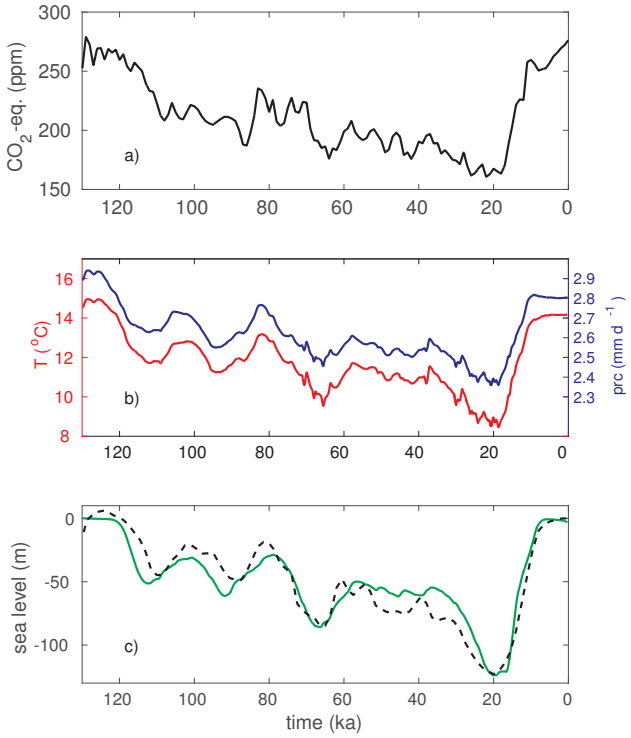

Figure 1. Reference simulation of last glacial cycle with CLIMBER-2 model coupled with SICOPOLIS model via SEB approach. **(a)** Driving equivalent CO_2 concentration, **(b, red)** global mean surface air temperature, **(b, blue)** global mean precipitation and **(c)** sea level shown by **green line** from simulated ice volume variation and by **black dashed line** from reconstructions by Waelbroeck et al. (2002).

Table 1. Summary of PDD parameters inducing minimum rms–errors between series of offline A_{PDD} and A_{SEB} for American and European ice sheets covering entire glacial cycle (see Fig. 5), glacial phase and glacial termination (see Fig. 6).

		America	Europe
interval	σ	$(\alpha_S,\ \alpha_I)$	$(\alpha_S,\ \alpha_I)$
ka	°C	$\mathrm{mm\,°C^{-1}d^{-1}}$	$\mathrm{mm\,°C^{-1}d^{-1}}$
130 – 0	3	(10, 16)	(5, 16)
130 –30	3	(8, 16)	(5, 16)
30 – 0	3	(10, 16)	(6, 16)
130 – 0	5	(5, 12)	(3, 14)
130 –30	5	(4, 10)	(4, 6)
30 – 0	5	(6, 12)	(3, 16)

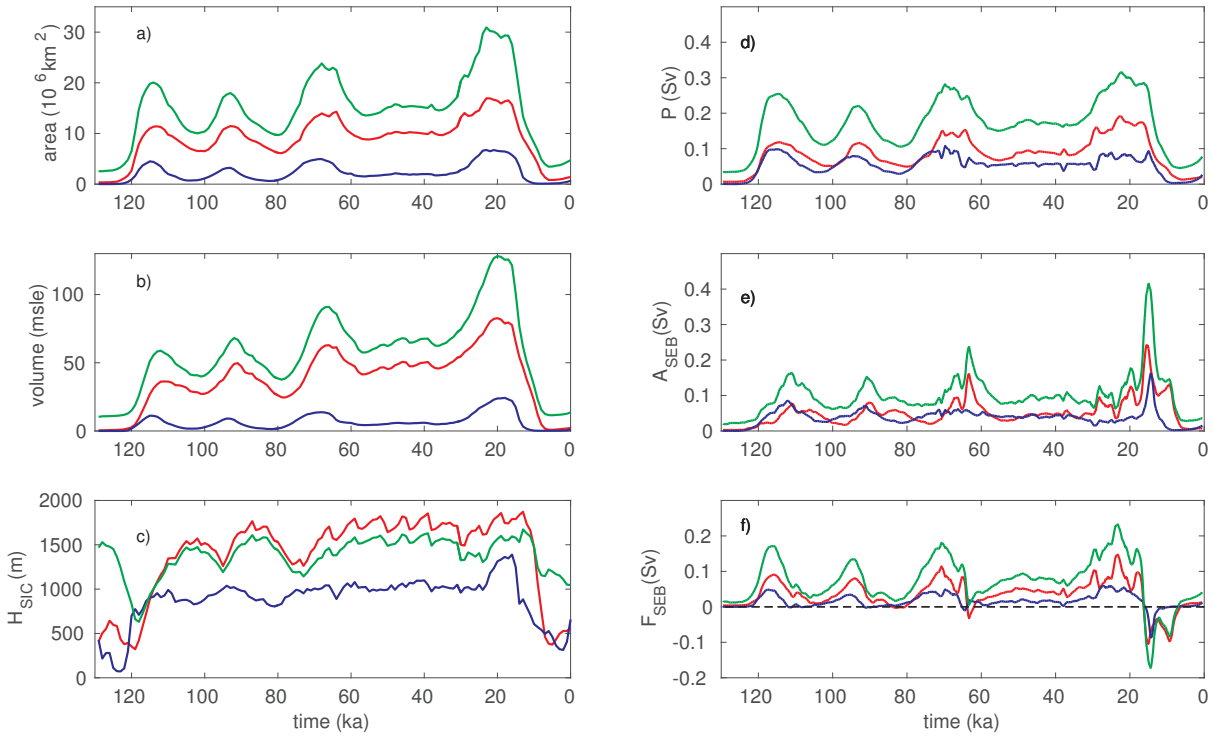

Figure 2. Glacial cycle series from reference simulation for NH total **(green lines)**, American **(red lines)** and European **(blue lines)** ice sheets showing **(a)** ice-covered area, **(b)** ice sheet volume, **(c)** average ice sheet thickness, **(d)** accumulation, **(e)** SEB-derived ablation and **(f)** surface ice mass balance.

Table 2. Ablation (in Sv) from NH total, American and European ice sheets at glacial termination (16–14 ka) where maximum in A_{SEB} at 15 ka for NH is closely reproduced with offline PDD method using σ=3 °C and (α_S, α_I)=(6, 19) in $\mathrm{mm\,^{\circ}C^{-1}d^{-1}}$ (see Fig. 7). But maxima in ablation (**bold**) occur a millennium earlier in A_{SEB} than in A_{PDD} for NH total and American ice sheets. Note, while the total ablation at 15 ka from both method are close, A_{SEB} in America is underestimated and A_{SEB} in Europe is overestimated by the PDD method.

time	NH		America		Europe	
ka	A_{SEB}	A_{PDD}	A_{SEB}	A_{PDD}	A_{SEB}	A_{PDD}
16	0.37	0.32	**0.25**	0.18	0.07	0.08
15	**0.41**	0.42	0.24	**0.19**	0.12	0.16
14	0.38	**0.45**	0.16	0.14	**0.18**	**0.24**

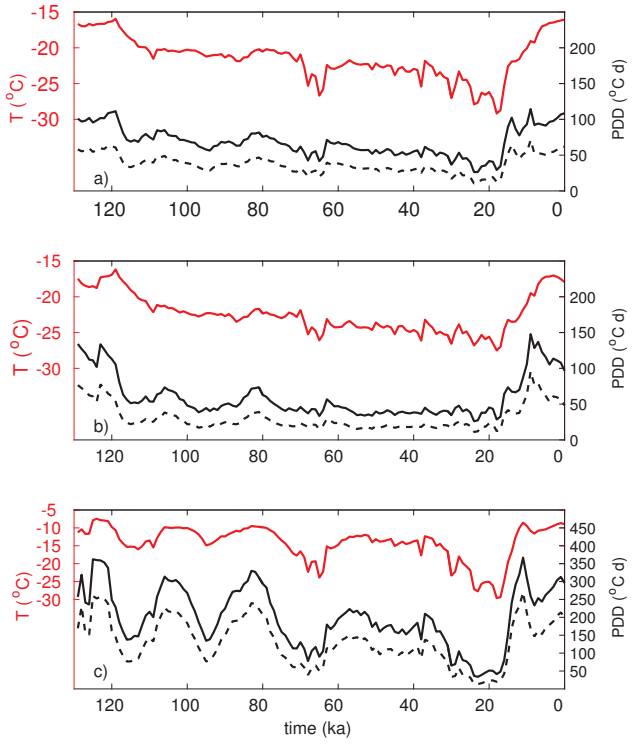

Figure 3. Glacial cycle series averaged over **(a)** NH total, **(b)** American and **(c)** European ice sheets showing on **left axes (red)** surface air temperature and on **right axes (black)** PDD values (Eq. 2) computed with σ=3 °C **(dashed lines)** and with σ=5 °C **(continuous lines)**.

Table 3. Global surface air temperature (T) and sea level (sl) at 21 ka (LGM) and 0 ka (MOD) from reference simulation (RS) compared with PDD-online simulations using σ in °C and (α_S, α_I) in mm °C^{-1}d^{-1}. PDD-online simulations are selected to fulfill the target windows glacial inception (I3, I5), glacial termination (T3, T5) and LGM (L3, L5) as shown in Fig. 10. Note, simulation I5 uses standard PDD parameter values (**bold**).

name	σ	(α_S, α_I)	T (°C)		sl (m)	
			LGM	MOD	LGM	MOD
RS			8.7	14.2	-122	-3.3
I3	3	(5, 16)	7.1	10.6	-263	-189
T3	3	(9, 16)	9.2	14.4	-94	-0.5
L3	3	(7, 20)	8.7	13.9	-121	-7.5
I5	**5**	**(3, 8)**	7.1	9.2	-255	-223
T5	5	(6, 8)	10.5	14.4	-31	-0.3
L5	5	(4, 7)	8.5	13.1	-120	-45

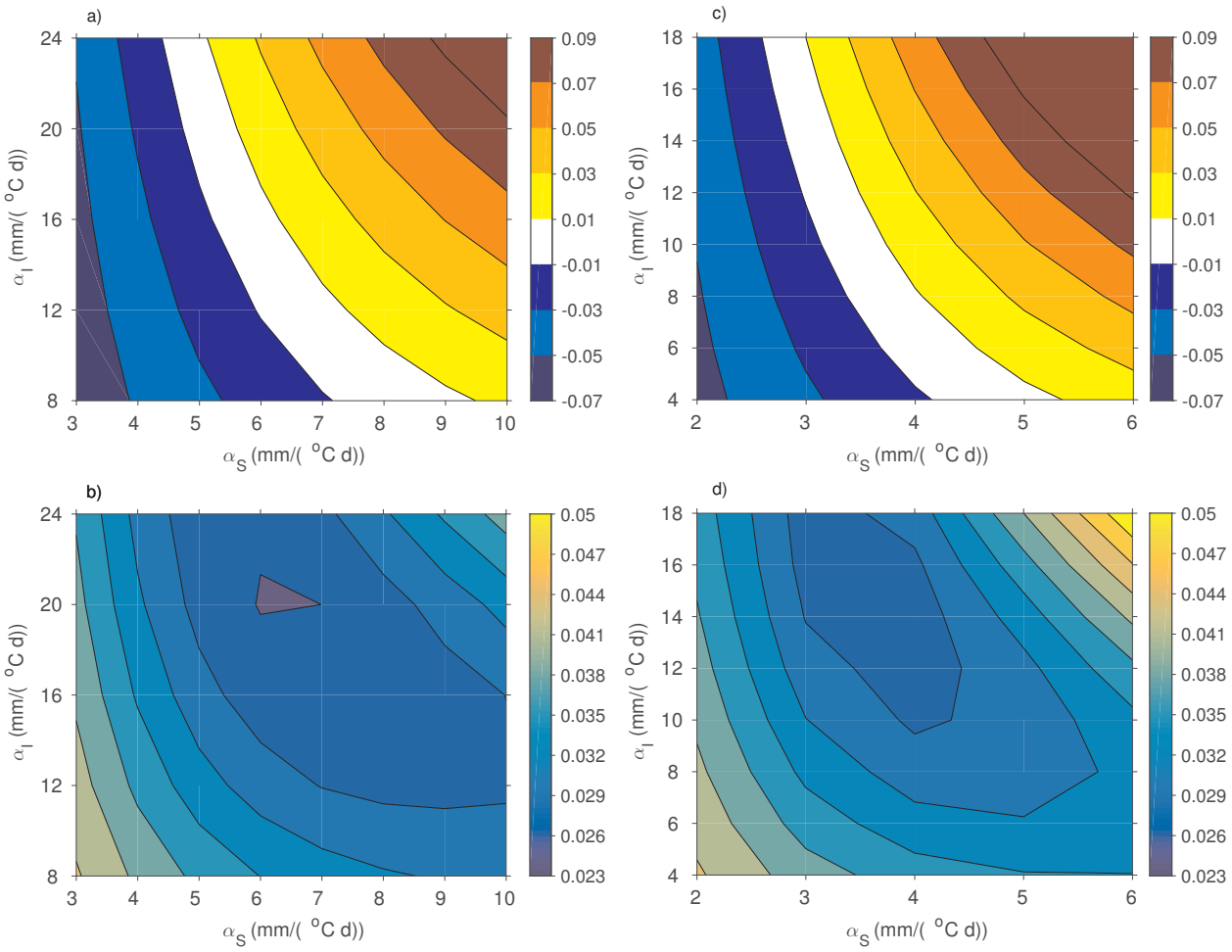

Figure 4. Bivariate distributions in **(a, c)** of mean anomaly m and in **(b, d)** of rms–error r (in Sv) from 130 ka-long NH ablation series as function of α_S and α_I using ensemble simulations of A_{PDD} (offline) relative to A_{SEB}. A_{PDD} simulations in **(a, b)** use σ=3 °C and in **(c, d)** σ=5 °C which involves larger values for (α_S, α_I) in **(a, b)** than in **(c, d)**. See Tab. 1 for PDD parameter values at minimum of rms–error in **(b, d)**.

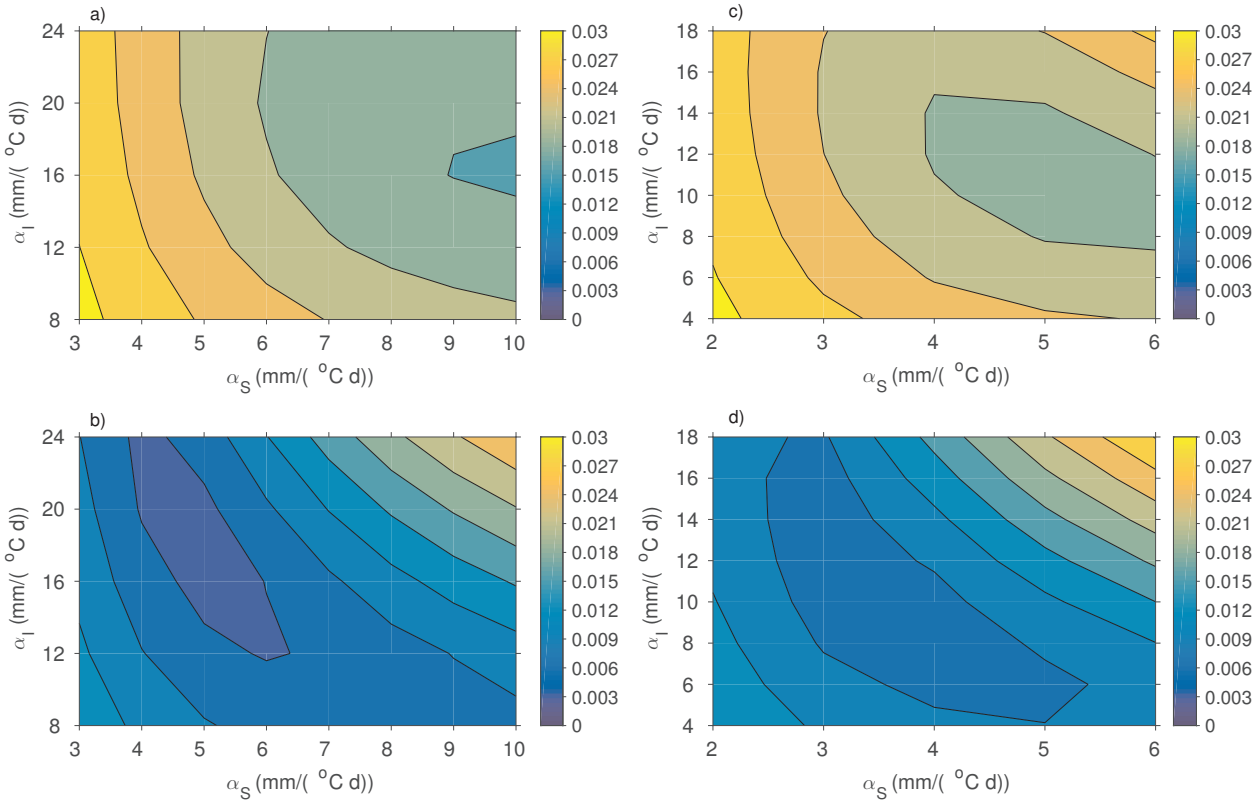

Figure 5. Bivariate distributions of rms–error r (in Sv) from 130 ka-long ablation series as in Fig. 4 but separately for **(a, c)** for American ice sheet in **(a, c)** and for European ice sheet in **(b, d)**. A_{PDD} simulation in **(a, b)** with σ=3 °C and in **(c, d)** with σ=5 °C. See Tab. 1 for PDD parameter values at minimum of rms–error in each panel.

Table 4. Global surface air temperature (T) and sea level (sl) at 21 ka (LGM) and 0 ka (MOD) from reference simulation (RS) with dust deposition ($Dust$), pure snow aging (Age_p) and aging of impure snow (Age_i) compared with online simulations using in C1 pure snow without pure snow aging (where simulation collapsed), in C2 snow with dust deposition without snow aging, in C3 pure snow with pure snow aging and in C4 snow with dust deposition and only pure snow aging. Note that simulation C1 collapsed.

name	$Dust$	Age_p	Age_i	T (°C)		sl (m)	
				LGM	MOD	LGM	MOD
RS	Y	Y	Y	8.7	14.2	-122	-3.3
C1	N	N	N	–	–	–	–
C2	Y	N	N	5.9	8.8	-322	-276
C3	N	Y	N	5.4	8.5	-356	-325
C4	Y	Y	N	7.2	10.7	-259	-151

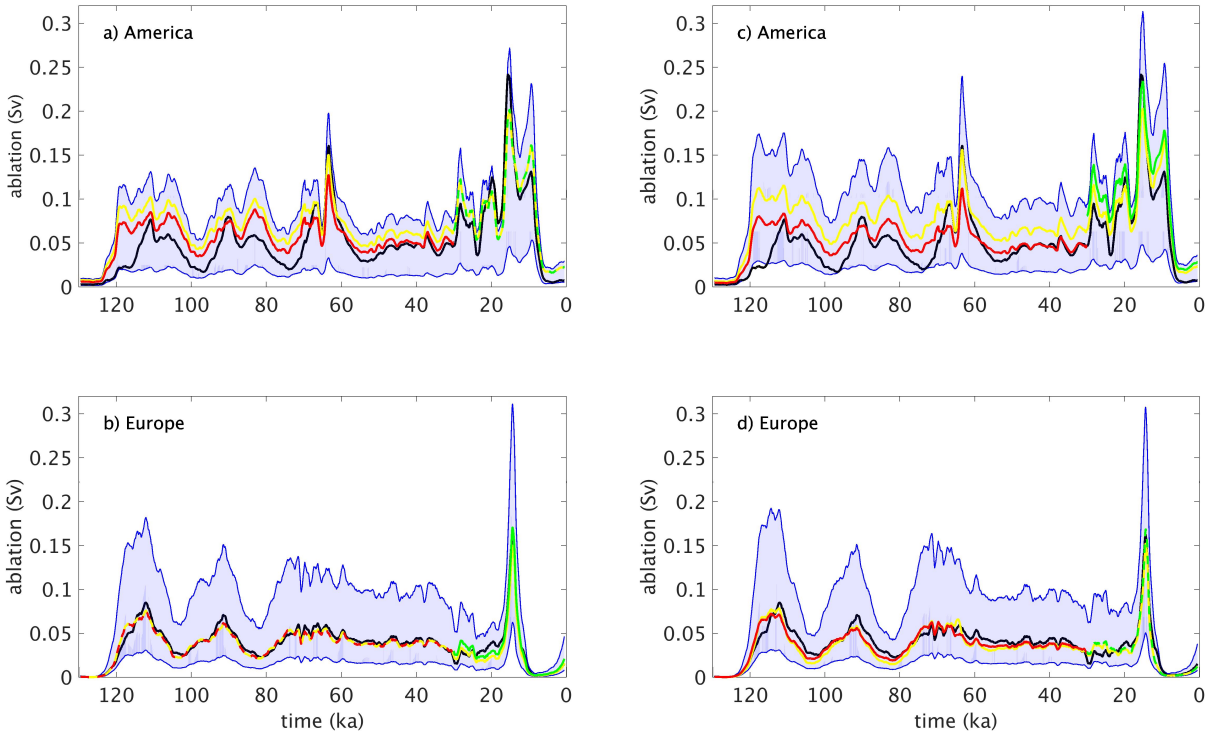

Figure 6. Glacial cycle series of ablation in **(a, c)** for American and in **(b, d)** for European ice sheets comparing offline A_{PDD} from full range of ensemble simulations **(blue shaded areas)** with A_{SEB} of reference simulation **(black lines)**. **(a, b)** shows A_{PDD} with σ=3 °C and **(c, d)** with σ=5 °C. PDD parameter values (σ, (α_S, α_I)) in (°C, (mm °C^{-1} d^{-1})) used for lower and upper boundary are in **(a, b)** (3, (3,8)) and (3, (10,24)), respectively, and in **(c, d)** (5, (2,4)) and (5, (6,18)), respectively. Further A_{PDD} series are shown which minimize rms–errors for American and European ice sheets over 130–0 ka (**yellow lines**), 130–30 ka (**red lines**) and 30–0 ka (**green lines**). PDD parameter values used in (**a**) **yellow**: (3, (10,16)), **red**: (3, (8,16)) and **green**: (3, (10,16)), in (**b**) **yellow**: (3, (5,16)), **red**: (3, (5,16)) and **green**: (3, (6,16)), in (**c**) **yellow**: (5, (5,12)), **red**: (5, (4,10)) and **green**: (5, (6,12)) and in (**d**) **yellow**: (5, (3,14)), **red**: (5, (4,6)) and **green**: (5, (3,16)). See Tab. 1 for summary of PDD parameter values at minima of r.

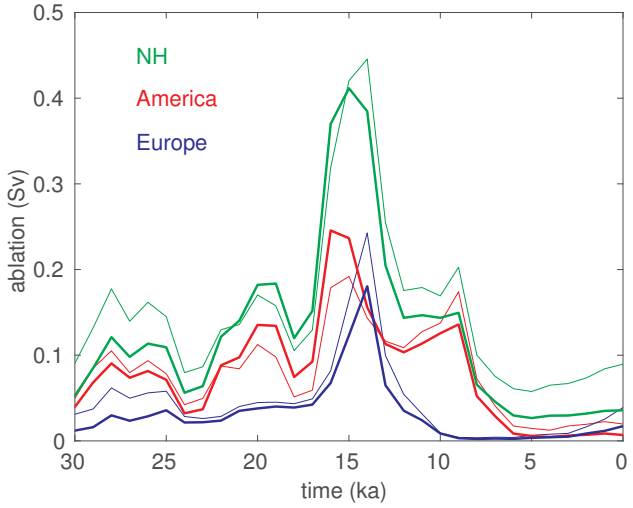

Figure 7. Ablation series from interval 30–0 ka for NH total (**green lines**), for American (**red lines**) and for European (**blue lines**) ice sheets showing A_{SEB} of reference simulation by **thick lines** and offline A_{PDD} by **thin lines**. A_{PDD} with σ=3 °C and $(\alpha_S\ \alpha_I)$= (9, 16) mm °C^{-1} d^{-1} is compatible with A_{SEB} at 15 ka. See Tab. 2 for peak ablation values.

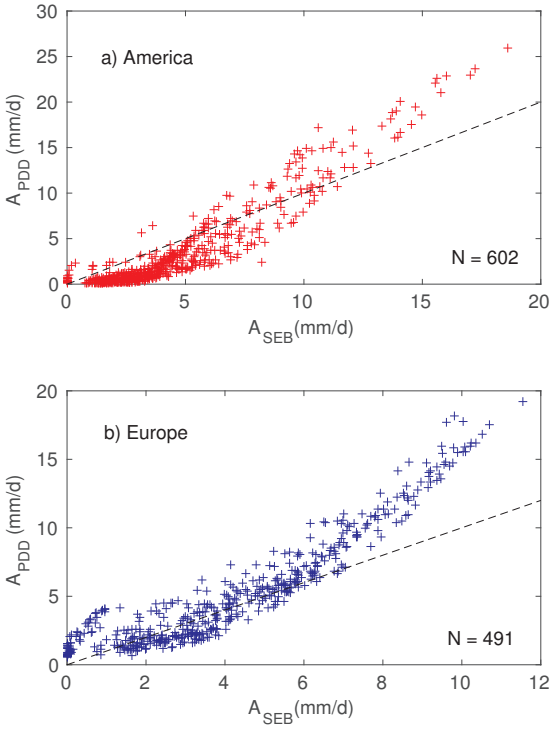

Figure 8. Scatter diagram of ablation rates by PDD method (offline) and SEB method from **(a)** American and **(b)** European ice sheets at 15 ka with equal NH ablation from both methods as shown in Fig. 7. N is number of SICOPOLIS grid cells with non-zero ablation rate.

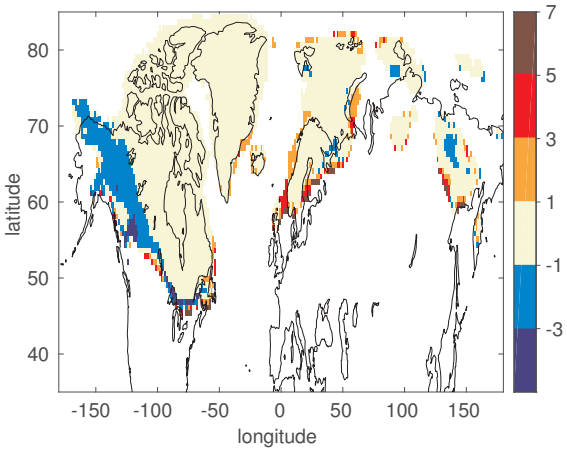

Figure 9. Geographic distribution of ablation differences (in $\mathrm{mm\,d^{-1}}$) obtained from PDD offline simulation using σ=3 $^\circ$C and (α_S α_I)= (9, 16) $\mathrm{mm\,^\circ C^{-1}\,d^{-1}}$ relative to reference simulation at 15 ka, where NH total ablation from PDD and SEB methods agree closely (see Fig. 7). Thin black lines are present day coastlines.

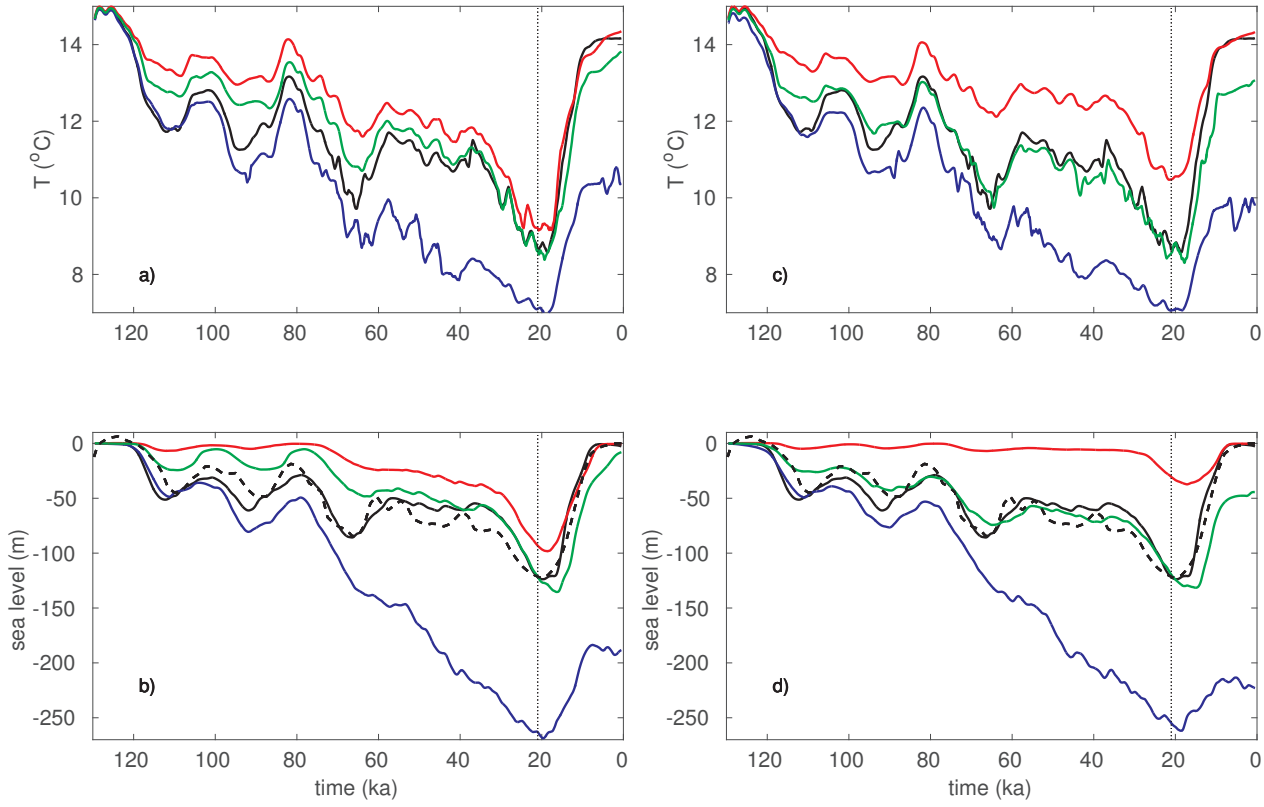

Figure 10. Glacial cycle simulations with online PDD method (**colored lines**) compared to reference simulation (**black continuous line**, cf. Fig. 1). **(a, c)** show global mean temperature and **(b, d)** show sea level together with reconstructed sea level **(black dashed line)**. PDD-online simulations in **(a, b)** with σ=3 °C and in **(c, d)** with σ=5 °C reproduce climate closely either at inception (**blue lines**) or at termination (**red lines**) or at LGM (**green lines**). Melt factors (α_S, α_I) in $\mathrm{mm\,^{\circ}C^{-1}\,d^{-1}}$ used in **(a, b)** for simulations I3 (**blue**), T3 (**red**) and L3 (**green**) are (5,16), (9,16) and (7,20), respectively, and used in **(c, d)** for simulations I5 (**blue**), T5 (**red**) and L5 (**green**) are (3,8), (6,8) and (4,7), respectively. Note, simulation I5 uses standard PDD parameters and generates excessive cooling without recurrence to Holocene climate. Vertical dotted line marks 21 ka. See Tab. 3 for global mean T and sea level at 21 and 0 ka.

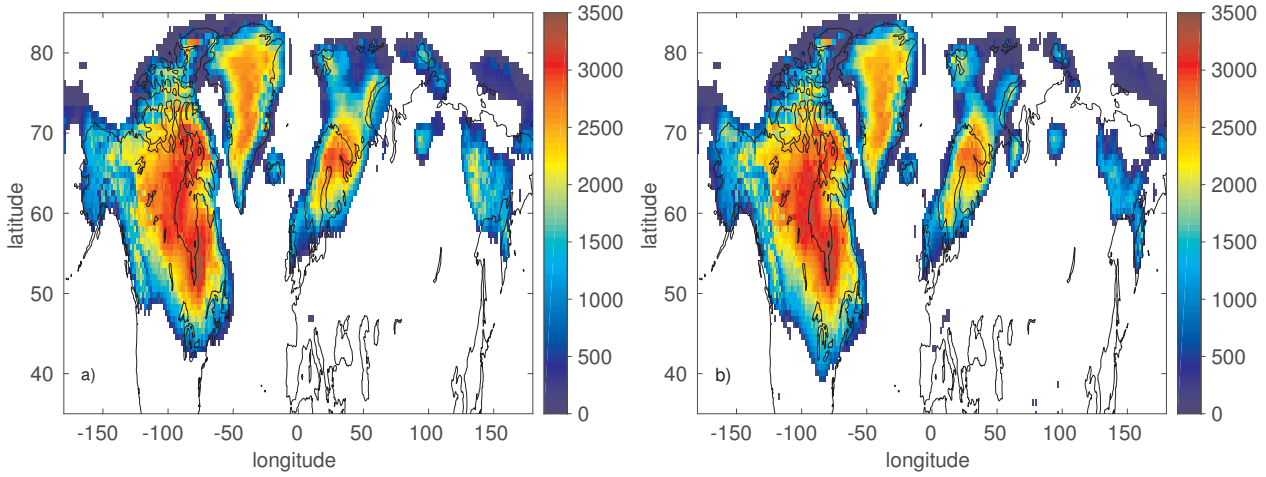

Figure 11. Simulated ice sheet thickness (in m) at 21 ka from **(a)** reference and **(b)** PDD-online simulation L3 which fulfills the LGM target window (see Tab. 3 and Fig. 10 for PDD parameter values). Thin black lines are present day coastlines.

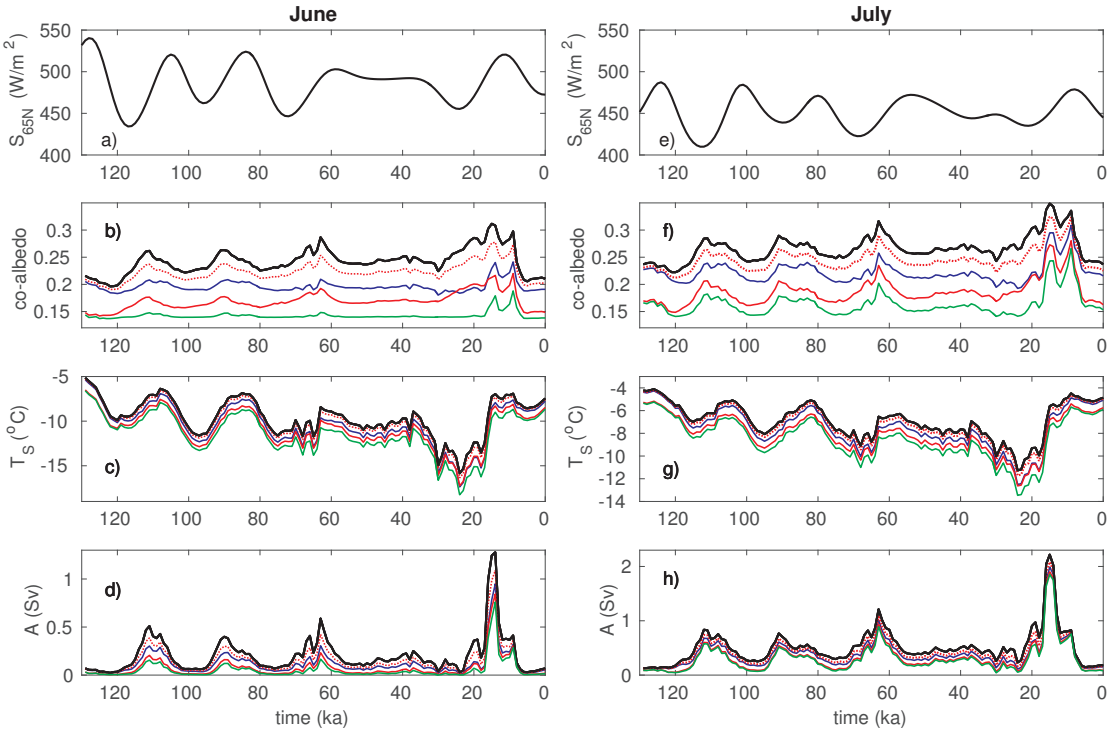

Figure 12. Monthly mean time series for June (**a - d**) and July (**e - h**) of top-of-atmosphere insolation at 65 °N and of simulated averages over NH ice sheets of co-albedo at surface in (**b, f**), surface temperature in (**c, g**), and ablation in (**d, h**). **Black lines** represent references of standard model and **colored lines** are offline simulations with modified snow albedo used in SEB approach (see Tab. 4) showing C1 with pure snow and no snow aging in **green**, C2 with dust deposition and no snow aging in **red**, C3 with pure snow and snow aging in **blue** and C4 with dust deposition and only pure snow aging in **red, dotted**. Note y-scaling in (**c, g**) and in (**d, h**) differ.

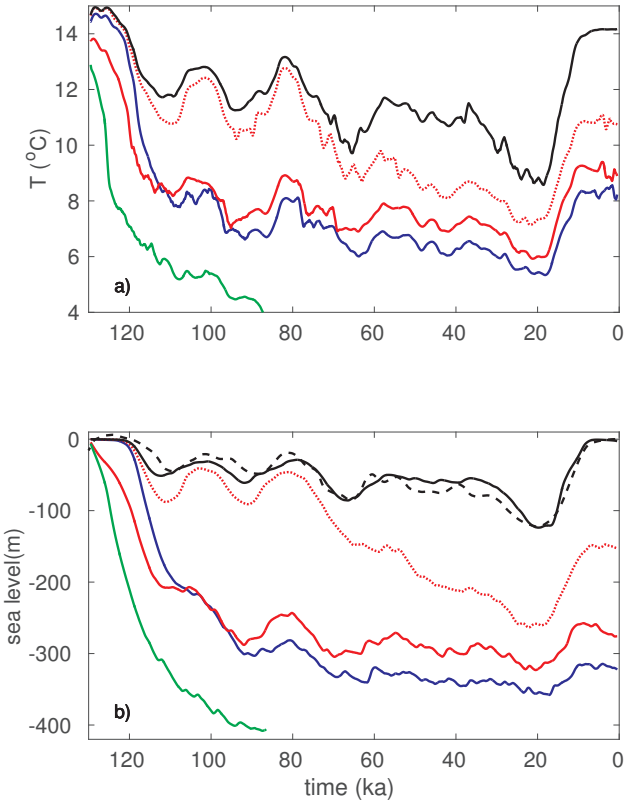

Figure 13. Glacial cycle series of temperature (**a**) and sea level (**b**) from online simulations with modified snow albedo as in Fig. 12.